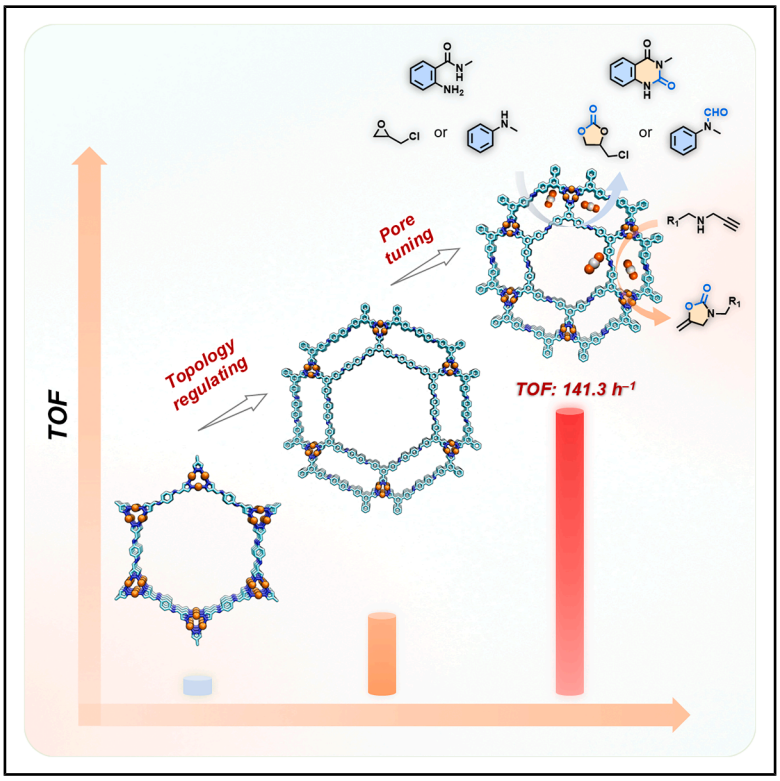
Chem

Article

Regulating the topology and pore size of covalent metal-organic frameworks for boosting catalytic CO_2 conversion

Graphical abstract



Highlights

- Controlled topology and pore size of the CMOF led to enhanced CO_2 capture and conversion
- The CMOF can catalyze multiple distinct CO_2 conversion reactions
- The CMOF maintains high CO_2 conversion activity under humid, complex flue gas

Authors

Xu Chen, Yu-Yang Li, Zhi-Hong Lin, ..., Hai-Long Jiang, Guo-Hong Ning, Dan Li

Correspondence

guohongning@jnu.edu.cn

In brief

Tuning the topology and pore size of covalent metal-organic frameworks (CMOFs) can significantly boost their performance in converting CO_2. Heteropore structures and reduced pore sizes dramatically enhance CO_2 uptake and activity, even under humid flue gas conditions, providing a clear design strategy for efficient carbon capture and conversion.

Chen et al., 2026, Chem *12*, 103006
October 8, 2026 © 2026 Elsevier Inc. All rights are reserved, including those for text and data mining, AI training, and similar technologies.
https://doi.org/10.1016/j.chempr.2026.103006

CellPress

Chem

CellPress

Article

Regulating the topology and pore size of covalent metal-organic frameworks for boosting catalytic CO_2 conversion

Xu Chen,[1,4] Yu-Yang Li,[2,4] Zhi-Hong Lin,[1] Jing-Yi Song,[1] Ri-Qin Xia,[1] Chuang-Wei Zhou,[1] Yu-Mei Wang,[1] Yu Han,[3] Hai-Long Jiang,[2] Guo-Hong Ning,[1,5,*] and Dan Li[1]

[1]State Key Laboratory of Bioactive Molecules and Druggability Assessment, Guangdong Provincial Key Laboratory of Supramolecular Coordination Chemistry, College of Chemistry and Materials Science, Jinan University, Guangzhou 510632, China

[2]Hefei National Research Center for Physical Sciences at the Microscale, School of Chemistry and Materials Science, University of Science and Technology of China, Hefei, Anhui 230026, China

[3]Center for Electron Microscopy, School of Emergent Soft Matter, State Key Laboratory of Pulp and Paper Engineering, South China University of Technology, Guangzhou 510640, China

[4]These authors contributed equally

[5]Lead contact

*Correspondence: guohongning@jnu.edu.cn

https://doi.org/10.1016/j.chempr.2026.103006

THE BIGGER PICTURE Considerable attention has been directed to metal-organic frameworks (MOFs) as a promising platform for carbon dioxide (CO_2) capture and conversion. Conventionally, the incorporation of multiple active metal sites, defect engineering, induction of functional groups (e.g., halogens, bases, and sulfones), and pre-installation of guests (e.g., metal-based nanoparticles and ionic liquid) have been employed to enhance the efficiency of MOF-based catalysts for CO_2 conversion. Here, we pioneered a novel approach to enhance MOFs for CO_2 capture and conversion by tuning their topology and pore size. Employing this approach, we synthesized a family of two-dimensional (2D) heteropore covalent MOFs (CMOFs) that proved to be highly efficient catalysts for various CO_2 conversion reactions, including the carboxylative cyclization of propargylamine or epoxides, the conversion of CO_2 into quinazoline-2,4(1*H*,3*H*)-diones, and the *N*-formylation of amines. This approach establishes a precedent for the molecular-level design of 2D heteropore MOFs, thereby unlocking their potential as a multifunctional platform for efficient CO_2 conversion catalysis.

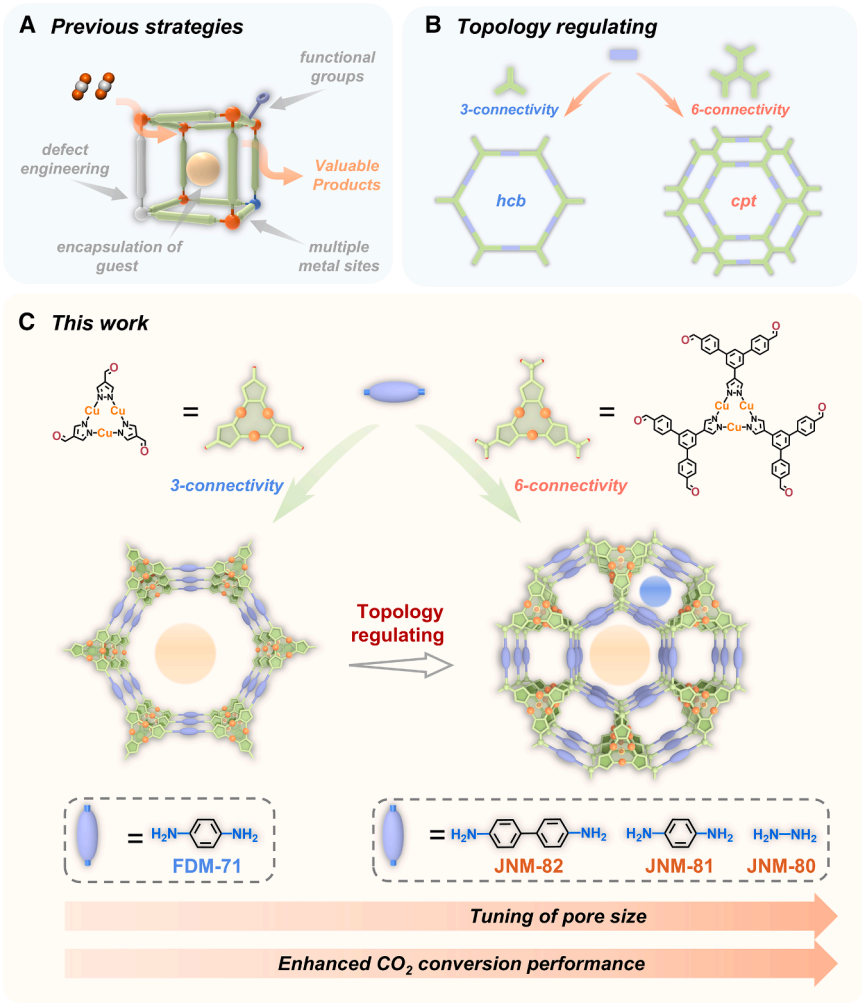
SUMMARY

The development of porous materials that serve as low-cost and efficient heterogeneous catalysts for CO_2 conversion under dilute conditions is highly desirable yet challenging. Herein, we demonstrated the improvement of the catalytic performance of covalent metal-organic frameworks (CMOFs) for carbon dioxide (CO_2) conversion by strategically regulating their topology and pore size—an underexplored approach for MOF catalysts. By modifying pyrazolate ligands, the topology was mediated from a homopore *hcb* structure to a heteroporous *cpt* network. Furthermore, varying the length of diamine ligands enabled precise pore-size tuning. Interestingly, heteropore CMOFs exhibited superior CO_2 uptake and catalytic activity compared with homopore analogs. Notably, reducing the pore size further strengthened CO_2 affinity and boosted catalytic performance in various CO_2 conversion reactions. The optimized catalysts also maintained high activity under humid conditions with simulated flue gas. Mechanistic studies involving nuclear magnetic resonance (NMR) monitoring, isotope labeling, density functional theory (DFT), and grand canonical Monte Carlo (GCMC) calculations provide insights into the catalytic process.

INTRODUCTION

The escalating levels of carbon dioxide (CO_2) emissions, the primary greenhouse gas driving climate change, pose severe environmental challenges worldwide.[1–3] One sustainable approach for reducing CO_2 emissions is to utilize CO_2 as a C1 building block for the synthesis of value-added chemicals and fuels, such as CO_2 reduction products, starch, cyclic carbonates, and 2-oxazolidinones.[4–6] However, the inherent thermodynamic stability of CO_2 arising from its strong C=O bonds necessitates

All rights are reserved, including those for text and data mining, AI training, and similar technologies.



Scheme 1. Strategies for enhancing MOF-catalyzed CO_2 conversion performance

(A) Previous strategies for enhancing the catalytic performance of MOF-catalyzed CO_2 organic transformation.

(B) The underlying principle of topology regulation from ***hcb*** to ***cpt***.

(C) Our work: enhancing CO_2 conversion catalysis in MOFs via topology and pore size regulation.

the use of noble metals and/or energy-intensive conditions for effective conversion.[7,8] Moreover, most reported studies are performed under pure CO_2 atmosphere or high-pressure conditions,[9] which limits their practical applicability. Therefore, it is imperative to develop highly efficient, non-noble metal catalysts that can operate under low CO_2 concentrations and mild conditions, yet it remains highly challenging.

Metal-organic frameworks (MOFs) have emerged as versatile heterogeneous platforms for CO_2 capture and conversion, owing to their structural and chemical tunability, abundant open metal sites, and adjustable pore space.[9–18] So far, various strategies, such as the incorporation of multiple active metal sites,[19,20] defect engineering,[21] induction of functional groups (e.g., halogens, bases, and sulfones), and pre-installation of guests (e.g., metal-based nanoparticles and ionic liquid),[22] have been employed to enhance the efficiency of MOF-based catalysts for CO_2 conversion (Scheme 1A). It has been found that MOFs containing small pores or even ultra-micropores (less than 0.6 nm) can facilitate strong host-CO_2 interactions and thus enhance the local CO_2 concentration at catalytically active sites, resulting in boosting catalytic performance.[11,23] However, the diffusion of CO_2 and reactants is much slower within smaller pores than in larger ones,[24] leading to the significant decline in catalytic performance. Inspired by hierarchical reticular materials,[25–32] it is envisioned that the incorporation of both adjustable micropores and interconnected mesopores into MOFs could address the abovementioned dilemma. Specifically, micropores enrich the density of active sites and boost CO_2 adsorption capacity, meanwhile mesoporous channels facilitate CO_2 and reactant diffusion.

So far, a series of strategies have been explored to construct 2D heteropore frameworks, including angle-specific vertex,[27] desymmetrization,[28] multiple-linking site,[33] and mixed linker.[34] Employing a multiple-linking-site strategy, an increase in connectivity from 3- to 6-connected building blocks can convert the ***hcb*** topology into the ***cpt*** topology (Scheme 1B). Recently, we reported a class of 2D crystalline porous covalent MOFs (CMOFs) with ***hcb*** topology and homopore structure, which are constructed from coinage metal-based cyclic trinuclear units (M-CTUs, M = Cu, Ag, Au) as building blocks and networked via dynamic covalent chemistry (DCC).[35–39] Herein, we rationally designed a di-aldehyde pyrazole ligand and successfully synthesized three 2D heteropore Cu-CTU-based CMOFs with ***cpt*** topology, denoted as **JNM-80**, **JNM-81**, and **JNM-82** (**JNM** = Jinan materials) (Scheme 1C). For comparison, the homopore Cu-CTU-based CMOF, Fudan materials (FDM)-71,[40] has also been prepared. Interestingly, by regulating the topology of CMOFs, CO_2 adsorption capacity (i.e., 34.50 $cm^3\ g^{-1}$) of **JNM-80** was remarkably higher than that of FDM-71 (i.e., 14.73 $cm^3\ g^{-1}$). Notably, among the three heteropore CMOFs, **JNM-80** exhibited the highest CO_2 adsorption capacity and catalytic activity for carboxylative cyclization of propargylamine, conversion of CO_2 into quinazoline-2,4(1*H*,3*H*)-diones, cyclization of epoxides, and *N*-formylation of amines—further evidencing that the incorporation of smaller pores is beneficial for improving the catalytic activity. Remarkably, **JNM-80** maintained high catalytic activity even with simulated flue gas containing only 25% CO_2, 4% O_2, and 0.5% SO_2 under 90% humid conditions, affording up to 84% isolated yields across eight

samples. It also preserved both catalytic performance and structural integrity over seven consecutive catalytic cycles. Mechanism investigations obtained via nuclear magnetic resonance (NMR) monitoring, isotope labeling experiments, density functional theory (DFT), and grand canonical Monte Carlo (GCMC) calculations support the rational design principles underlying these materials. Our work establishes a novel molecular-level design strategy for 2D heteropore MOFs and demonstrates their potential as efficient and durable heterogeneous catalysts for CO_2 valorization.

RESULTS AND DISCUSSION

Syntheses and characterization

To construct heteropore CMOFs, the target ligand 5′-(1*H*-pyrazol-4-yl)-[1,1′:3′,1″-terphenyl]-4,4″-dicarbaldehyde (**1**) was synthesized (see supplemental information for details and Scheme 1C). The coordination reaction and Schiff-base condensation of Cu_2O, HL (**1**), and di-amine linkers (i.e., N_2H_4, *p*-phenylenediamine [PPD] or 4,4′-diaminobiphenyl [DABP]) under solvothermal conditions afforded the highly crystalline powders of **JNM-80**, **JNM-81**, and **JNM-82**, respectively (Scheme 1C; Figures S3–S5). For comparison, FDM-71 with homopore was synthesized according to the reported procedure (Figures S1 and S2).[40] The chemical structures of **JNMs** were elucidated via Fourier transform infrared spectroscopy (FTIR) and solid-state ^{13}C cross-polarization magic angle spinning NMR (CP/MAS NMR). As shown in Figure S6, the formation of imine bonds is confirmed by the emergence of a distinct stretching vibration peak of C=N at around 1,621–1,626 cm^{-1}. Moreover, the characteristic resonance peaks of imine carbons at ~157–161 ppm that were observed in the **JNMs** further evidence the successful formation of imine linkages (Figure S7). X-ray photoelectron spectroscopy (XPS) analysis confirmed the monovalent oxidation state of Cu in **JNMs**. Specifically, the XPS spectra of **JNMs** exhibited distinct peaks at ~932.5 and 952.4 eV, corresponding to Cu(I) $2p_{3/2}$ and $2p_{1/2}$, respectively, with no observable Cu(II) satellite peaks (Figure S8). Furthermore, the high-resolution XPS spectra of N 1s for the **JNMs** were analyzed. A single peak is observed at 399.3 eV, which is assigned to the pyrazole N of Cu-CTU, and another new single peak related to the imine N has a binding energy of approximately 400.5 eV (Figure S9). Scanning electron microscopy (SEM) images of the three **JNMs** consistently reveal a layered morphology (Figure S10). Energy dispersive X-ray mapping of **JNMs** shows a uniform distribution of Cu, C, and N elements throughout the samples (Figure S11).

Crystal structure and porosity

The long-distance-ordered structures of the as-prepared **JNMs** were investigated by powder X-ray diffraction (PXRD) analysis, and theoretical simulations were conducted using the Materials Studio 2019. All **JNMs** exhibit highly crystalline, heteropore isoreticular frameworks adopting a ***cpt*** topology with eclipsed layer stacking. For **JNM-80**, diffraction peaks at 2.52°, 4.33°, 5.02°, 7.55°, and 8.73° were assigned to the (100), (110), (200), (300), and (220) crystallographic planes, respectively (Figure 1A). Pawley refinements of **JNM-80** generated a unit cell with a space group of *P*6/m with residual factors of R_p = 5.60% and R_{wp} = 3.71% (cell parameters: $a = b$ = 40.5806 Å, c = 3.4384 Å) (Figures 1A and 1D; Table S1). In contrast, staggered AB and ABC stacking were inconsistent with the experimental data (Figures S12–S14; Tables S2 and S3). Similarly, Pawley refinement of **JNM-81** and **JNM-82** indicated that both exhibited AA-stacked interlayer arrangements and crystalized in the *P*6/m space group with good agreement factors (i.e., R_p = 3.63% and R_{wp} = 2.61% for **JNM-81**, R_p = 2.82% and R_{wp} = 2.11% for **JNM-82**, respectively) (Figures 1B, 1C, 1E, 1F, and S15–S20; Tables S4–S9).

To further evidence the heteropore structure, the surface areas and pore size distributions of **JMNs** were determined via an N_2 adsorption-desorption isotherm at 77 K (Figure 1G). The Brunauer-Emmett-Teller (BET) surface areas of **JNM-80**, **JNM-81**, and **JNM-82** were determined to be 904.1, 388.3, and 561.3 $m^2\ g^{-1}$, respectively (Figure 1G). Pore distributions, obtained from non-local DFT (NLDFT) models, revealed two distinct distributions, indicative of the coexistence of micropores and mesopores. Specifically, the larger pore average diameters of **JNM-80**, **JNM-81**, and **JNM-82** were 2.5, 3.3, and 3.8 nm, respectively, consistent with their theoretical pore size (i.e., 2.4, 3.3, and 3.9 nm). Meanwhile, the smaller pore size of **JNM-80**, **JNM-81**, and **JNM-82** were 1.1, 1.4, and 1.3 nm, respectively, in good agreement with those of the simulated pseudo-hexagonal micropores (i.e., 0.8, 0.9, and 0.9 nm) (Figure 1H).

To validate the fidelity of the PXRD-based structural elucidation of the 2D CMOFs, high-resolution transmission electron microscopy (HR-TEM) was employed. The HR-TEM images (Figures 2A–2C, S21, and S22) displayed lattice fringe spacings of 3.72, 4.25, and 4.89 nm for **JNM-80**, **JNM-81**, and **JNM-82**, respectively. These values corresponded well with the *d*-spacing of the (1 0 0) reflection predicted for the heteropore models with AA stacking (3.58, 4.16, and 4.90 nm for **JNM-80**, **JNM-81**, and **JNM-82**, respectively), thus further confirming the predicted CMOF structures. Additionally, as shown in Figures 2E–2J, well-defined reticular structures featuring approximately hexagonal pores were observed. The distances between the centers of the two adjacent pores were 4.1 ± 0.1 and 4.9 ± 0.2 nm for **JNM-81** and **JNM-82**, respectively, which were in good agreement with the simulated values. The TEM analysis further corroborated that the synthesized **JNMs** exhibit the anticipated heteropore structures, consistent with those reported for heteropore frameworks.[28,34,41,42]

Stability and CO_2 adsorption

Thermogravimetric analysis (TGA) of **JNMs** revealed the moderate thermal stability, with no significant degradation observed up to 300°C under an N_2 atmosphere (Figure S23). In addition, the **JNMs** were soaked in various solvents, including C_2H_5OH, H_2O, *N*,*N*-Dimethylformamide (DMF), aqueous HCl (0.1 M), aqueous NaOH (15 M), and other common solvents, at room temperature for a duration of 3 days. The resulting PXRD patterns remained consistent with the original samples, demonstrating that these **JNMs** possess good chemical stability (Figure S24).

Since CO_2 adsorption capacity is a critical parameter in the catalytic conversion of CO_2,[43] the CO_2 sorption isotherms of

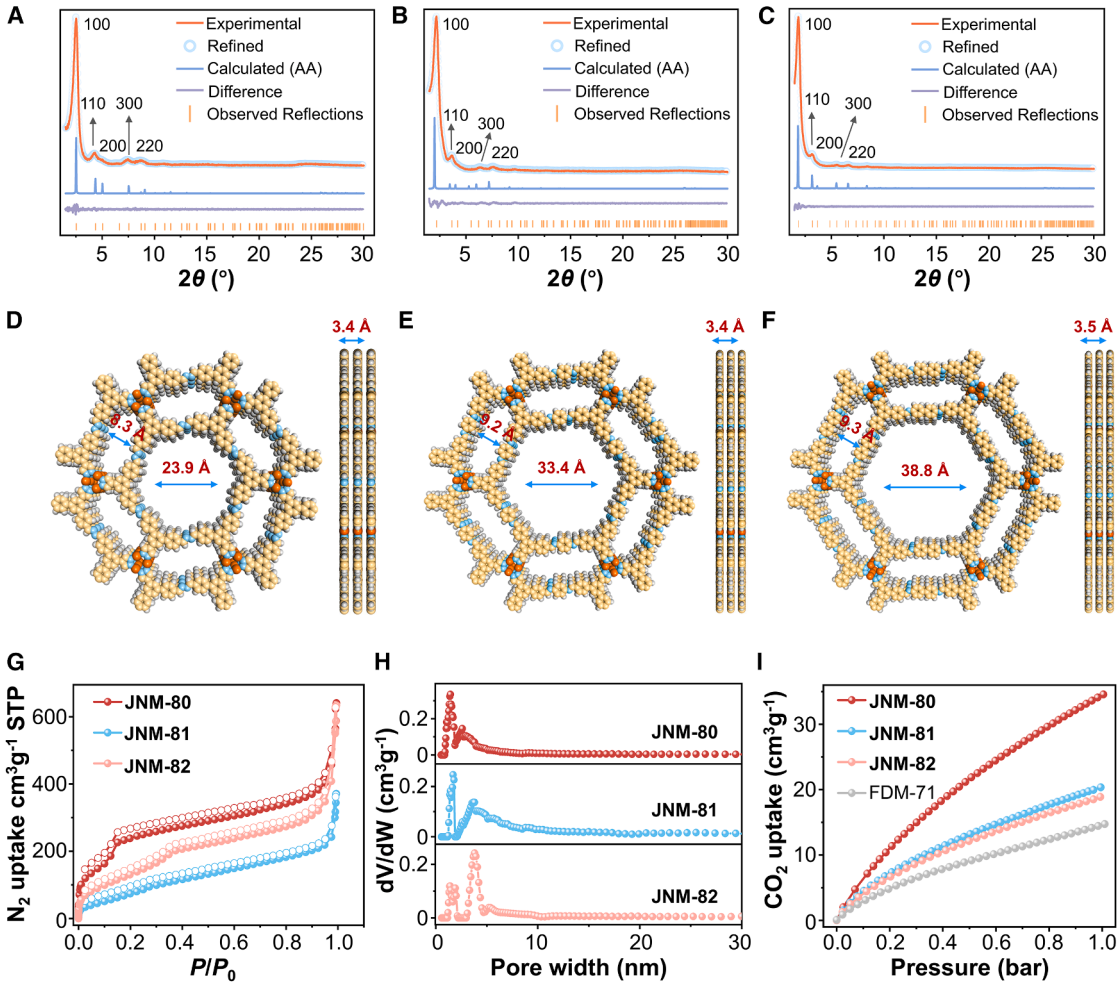


Figure 1. Crystal structure and porosity of JNM-80, JNM-81, and JNM-82

(A–C) PXRD structural analysis of (A) **JNM-80**, (B) **JNM-81**, and (C) **JNM-82** (experimental curve, orange line; Pawley refinement data, sky blue circle; simulated profile of AA packing mode, light blue line; difference plot, indigo blue line; Bragg positions, pale yellow line).

(D–F) Top (left) and side (right) views of the refined AA-stacking model of (D) **JNM-80**, (E) **JNM-81**, and (F) **JNM-82**.

(G) N_2 adsorption-desorption isotherms of **JNMs** at 77 K.

(H) The pore size distribution of **JNMs**.

(I) CO_2 sorption isotherms of **JNMs** at 273 K.

JNMs were measured and compared. Typically, **JNM-80**, **JNM-81**, **JNM-82**, and FDM-71 delivered the maximum CO_2 uptake capacities of 34.50, 20.36, 18.89, and 14.73 $cm^3\ g^{-1}$, respectively (Figure 1I), with **JNM-80** demonstrating the highest CO_2 affinity. Notably, despite the similar larger pore size of **JNM-80** and FDM-71, **JNM-80** exhibited a 2.34-fold increase in CO_2 uptake capacities, suggesting the smaller pores in the heteropore structure are beneficial for CO_2 adsorption. Moreover, with the length of di-anime linker increasing, the CO_2 uptake capacities remarkably decreased, implying that a smaller heteropore size is more favorable for CO_2 adsorption. This trend may be attributed to the fact that the increase in pore size may weaken the synergistic effect between adsorption sites, reducing the host-guest interaction and CO_2 adsorption performance.[44] Furthermore, it is well-established that the introduction of nitrogen-based Lewis base sites in COFs and MOFs enhances the CO_2 affinity.[11] Indeed, among these four CMOFs, **JNM-80** showed a higher density of nitrogen-based Lewis base sites, contributing to its superior CO_2 affinity. These findings position **JNM-80** as a promising heterogeneous catalyst for CO_2 conversion.

Heterogeneous catalysis

The high crystallinity, superior CO_2 adsorption capacity, and accessible copper sites of **JNMs** render them highly promising photocatalysts for the catalytic cyclization of propargylamine and CO_2. To establish optimal conditions, the carboxylative cyclization of N-benzylprop-2-yn-1-amine (**2a**) was first evaluated as a model reaction. Under ambient CO_2 pressure and solvent-free conditions, the desired 2-oxazolidinone product (**3a**) was obtained in an impressive 93% isolated yield using

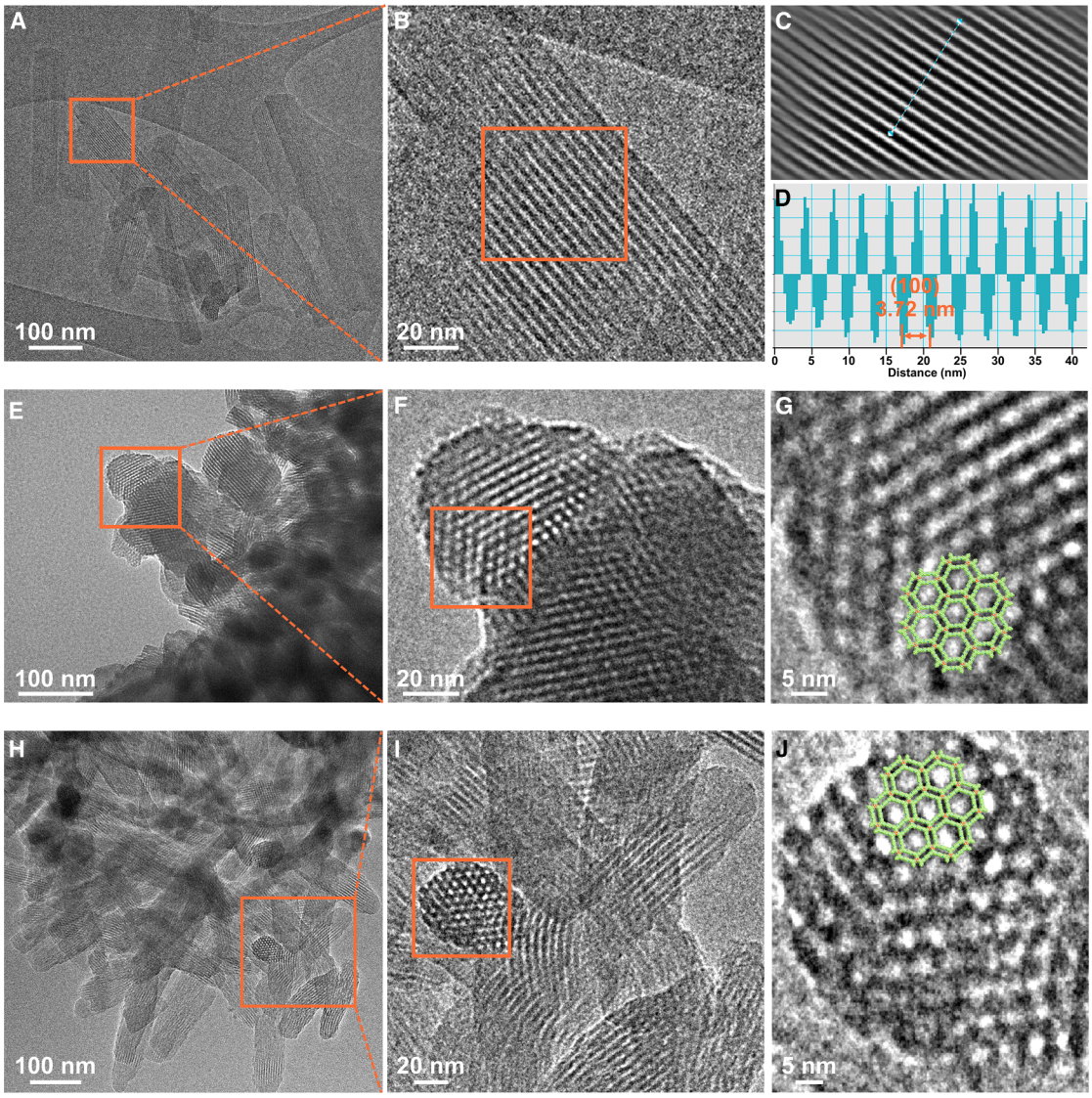


Figure 2. HR-TEM images of JNM-80, JNM-81, and JNM-82

(A, E, and H) HR-TEM images of (A) **JNM-80**, (E) **JNM-81**, and (H) **JNM-82**.

(B, F, and I) Enlarged image of a selected section in (A), (E), and (H).

(C and D) Inverse fast Fourier transform (IFFT) of **JNM-80** obtained from the selective areas in (B).

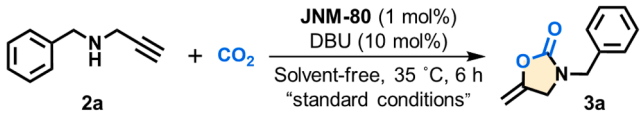
(G and J) Enlarged image of (G) **JNM-81** and (J) **JNM-82** from the marked area (F and I) with structure models inset.

1 mol % **JNM-80** as the catalyst and 10 mol % 1,8-diazabicyclo[5.4.0]undec-7-ene (DBU) as the base (Table 1, entry 1). The reaction exhibited negligible progress in the absence of **JNM-80** or DBU (Table 1, entries 2 and 3). Replacing DBU with alternative bases such as Et_3N, K_2CO_3, diisopropylamine (DIPA), or potassium tert-butoxide (*t*-BuOK) resulted in significantly reduced yield (Table 1, entries 4–7), underscoring the critical roles of both **JNM-80** and DBU. Switching the catalyst from **JNM-80** to Cu_2O dramatically decreased the yields to 7% (Table 1, entry 8). Similarly, employing FDM-71 as the catalyst afforded only 15% yield of **3a** (Table 1, entry 9), highlighting that the heteropore structure remarkably enhanced catalytic activity. Meanwhile, **JNM-81** and **JNM-82**, which incorporate longer organic linkers, produced desired products in lower yields of 62% and 40%, respectively (Table 1, entries 10 and 11). This decline may be attributed to their diminished CO_2 adsorption capacities.

Other CO_2-related reactions

To further verify the generality of heteropore CMOFs in promoting CO_2 conversion, we examined three additional transformations: the synthesis of quinazoline-2,4(1*H*,3*H*)-dione from CO_2 and aminobenzamides, the cyclization of epoxides, and the *N*-formylation of amines. Using 2-amino-*N*-methylbenzamide as a model substrate, the catalytic performance of **JNM-80** toward quinazoline-2,4(1*H*,3*H*)-dione formation was evaluated.

Table 1. Condition optimization of JNM-80-catalyzed carboxylative cyclization of N-benzylprop-2-yn-1-amine



Entry	Change from the "standard conditions"[a]	Yield (%)[b]
1	None	98 (93)[c]
2	no catalyst	<1
3	no DBU	3
4	Et_3N, instead of DBU	7
5	K_2CO_3, instead of DBU	5
6	DIPA, instead of DBU	12
7	*t*-BuOK, instead of DBU	16
8	Cu_2O, instead of **JNM-80**	7
9	FDM-71, instead of **JNM-80**	15
10	**JNM-81**, instead of **JNM-80**	62
11	**JNM-82**, instead of **JNM-80**	40
12	1 g scale	53[c]
13	dilute CO_2[d] instead of pure CO_2	93
14	flue gas[e] under 90% humidity instead of pure CO_2	82

[a]Reactions condition: **2a** (0.8 mmol), catalyst (1 mol %, based on Cu), CO_2 (1 atm), solvent-free, 35°C.
[b]Yields were determined by ^{1}H NMR spectroscopy with 1,1,2,2-tetrachloroethane as internal standard.
[c]Isolated yield.
[d]CO_2: 25%, N_2: 75%, P (1 atm), DBU (20 mol %), solvent-free, 50°C, 12 h.
[e]CO_2: 25%, N_2: 70.5%, O_2: 4%, SO_2: 0.5%, P (1 atm), DBU (20 mol %), solvent-free, 60°C, 12 h. Catalyst was exposed to humid conditions (relative humidity [RH]: 90%) for 12 h before the reaction.

Under ambient CO_2 conditions, with DBU and triphenyl phosphite ($P(OPh)_3$) as co-catalysts, **JNM-80** furnished the desired 3-methylquinazoline 2,4(1*H*,3*H*)-dione in 94% yield within 10 min (Figure S31). By contrast, **JNM-81**, **JNM-82**, and FDM-71 gave lower yields of 81%, 75%, and 59%, respectively (Figure S31). Similar trends were observed in both reactions. For epichlorohydrin cyclization, **JNM-80** achieved a 96% yield, higher than that of **JNM-81** (80%), **JNM-82** (72%), and FDM-71 (55%). Likewise, in the *N*-formylation of amines, the yield followed **JNM-80** (84%) > **JNM-81** (56%) > **JNM-82** (48%) > FDM-71 (39%) (Figures S32 and S33). Furthermore, as shown in Figures S31–S33, these reactions demonstrate high substrate tolerance. Collectively, these results demonstrate that the micropores within the heteropore CMOFs play a critical role in boosting catalytic activity in the carboxylative cyclization of CO_2.

Catalytic kinetics and gram-scale reactions

For the carboxylative cyclization of propargylamine, the catalytic kinetics of **JNM-80** were investigated through plotting the NMR yield of **3a** vs. reaction time. In the presence of **JNM-80**, the product was detected at a yield of 14% within 20 min, achieving quantitative conversion after 6 h (Figure 3A). By contrast, when **JNM-81** or **JNM-82** was employed as the catalyst, both lower yield and slower kinetics were observed, compared with **JNM-80**. Kinetic analysis revealed the following rate constant ratios: $k_{\mathbf{JNM\text{-}80}}/k_{\mathbf{JNM\text{-}81}}$ = 3.9 and $k_{\mathbf{JNM\text{-}80}}/k_{\mathbf{JNM\text{-}82}}$ = 6.4 (Figure S25). Moreover, the gram-scale reactions under optimal conditions using **JNM-80** afforded 1.2 g of **3a** in 53% yield (Table 1, entry 12), corresponding to a turnover frequency (TOF) of 141.3 h^{-1} (Figure 3B). This TOF value surpasses most reported homogeneous and heterogeneous catalysts and represents an order-of-magnitude enhancement over homopore FDM-71 (i.e., 13.3 h^{-1}) (Table S11).

Reusability and flue gas test

Recyclability constitutes a critical metric for heterogeneous catalysts in practical applications. Over seven catalytic cycles, **JNM-80** retained 87% yield (initial yield: 94%; Figure 3C) while preserving its crystallinity and structural integrity, as confirmed by PXRD patterns and XPS spectra (Figures 3D and S26). Moreover, the inductively coupled plasma-optical emission spectrometer (ICP-OES) analysis revealed that 0.2 wt % of Cu was leached from **JNM-80** after one catalytic cycle, further indicating the excellent stability of the catalyst. Inspired by the exceptional catalytic activity of **JNM-80** in the cycloaddition of propargylamine with CO_2, we further evaluated its efficiency under simulated flue gas (CO_2:N_2 = 25:75). Under simulated flue gas, solvent-free cyclization of **2a** at 60°C achieves 93% yield within 12 h (Tables 1, entry 13 and S10), demonstrating high catalytic efficiency even in diluted CO_2 environments. To further

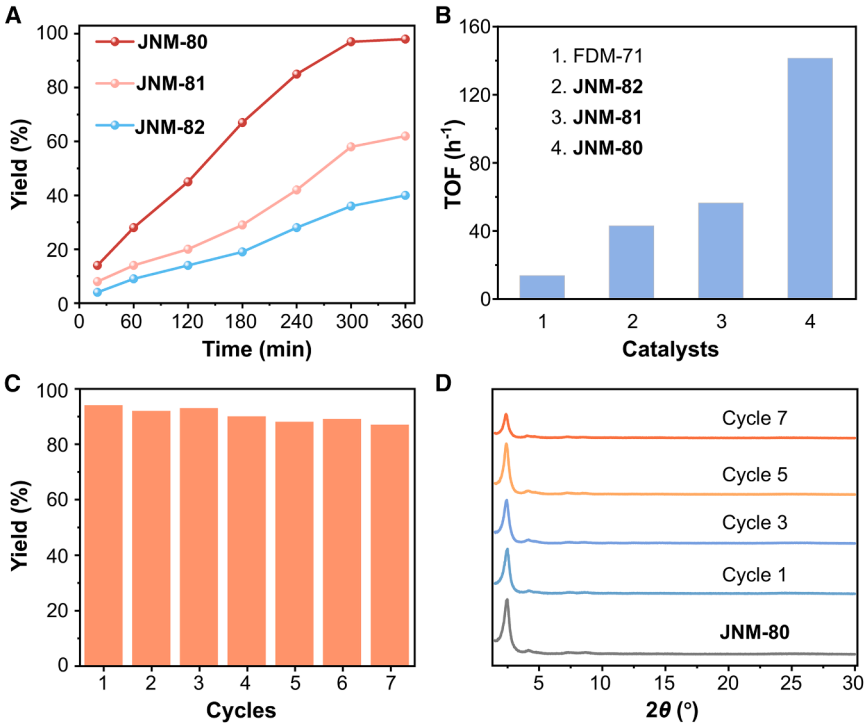


Figure 3. Catalytic kinetics, gram-scale, and reusability test

(A) Plots of yield vs. reaction time for **JNM-80**, **JNM-81**, and **JNM-82**.

(B) Comparison of TOF for the carboxylative cyclization of **2a** with CO_2 using FDM-71, **JNM-80**, **JNM-81**, and **JNM-82**.

(C) Recyclability of **JNM-80**-catalyzed carboxylative cyclization of **2a**. The yield is based on ^1H NMR analysis.

(D) PXRD patterns of **JNM-80** after seven catalytic cycles.

evaluate the catalyst's performance under simulated industrially relevant conditions, reactions were conducted using flue gas in a humid environment. Impressively, **JNM-80** delivered an 82% yield (Tables 1, entry 14 and S10) with simulated flue gas (CO_2: 25%, N_2: 70.5%, O_2: 4%, SO_2: 0.5%) at 90% humidity, and the structural integrity of the catalyst was maintained after the reaction (Figure S27). These results highlight its potential for direct conversion of industrial flue gas to value-added products.

Substrate scope

With the optimal reaction conditions established, we next explored the substrate scope using a variety of propargylic amines, summarized in Figure 4. Under pure CO_2, propargylic amines bearing electron-donating (**2a**–**2h**) or electron-withdrawing (**2i**–**2p**) *N*-benzyl substituents underwent carboxylative cyclization, affording the corresponding products in 62%–95% isolated yields. Furthermore, the propargylamines featuring heterocyclic (**2q** and **2r**) or alkyl substituents (**2s** and **2t**) were efficiently transformed, providing the desired products in 79%–91% yield. Notably, derivatives of pharmaceutically relevant molecules such as rasagiline (**2u**) and dehydroabietylamine (**2v**) derivatives also underwent efficient carboxylative cyclization, affording the target products in 83% and 69% yields, respectively. Remarkably, carboxylative cyclization reactions remained viable under simulated flue gas (initial CO_2 concentration: 25%) and high humidity, affording the corresponding products in moderate yields of 58%–84%. These results demonstrate that **JNM-80** can efficiently catalyze the cyclization of propargylamine even under low CO_2 concentration, providing an innovative, promising approach for the valorization and utilization of industrial flue gas into value-added chemicals.

Mechanism studies

To gain insight into the mechanism of this cyclization reaction, a series of mechanistic experiments were carried out. First, isotope labeling experiments were performed using $^{13}CO_2$ to clarify the origin of the carbon (Figure 5A). As shown in Figures 5B and S28, the formation of the carboxyl group in oxazolidinone was confirmed to originate from CO_2. Then, the reaction process was monitored through ^1H NMR spectroscopy (Figure 5C). Upon individual addition of **JNM-80** or DBU to a $CDCl_3$ solution of **2a**, no discernible change in the intensity of the alkyne proton signal (~2.28 ppm) was observed (Figure 5C). In contrast, when both **JNM-80** and DBU were charged, the signal of alkyne proton nearly disappeared, indicating that the propargylic amine can be synergistically activated via the combined action of **JNM-80** and DBU. Notably, the intensity of the alkyne proton exhibited only a minor reduction upon the substitution of **JNM-81**, **JNM-82**, or FDM-71 for **JNM-80** (Figure 5C). These results indicated that the introduction of heteropores into the framework and the regulation of the linker effectively promote propargylamine activation, thereby enhancing catalytic activity. Moreover, as the reaction proceeded, the characteristic signal of **2a** gradually diminished, while new peaks attributed to product **3a** emerged and progressively intensified (Figure S29), further elucidating the reaction pathway of the carboxylative cyclization of propargylamines with CO_2 catalyzed by **JNM-80**.

DFT and GCMC calculations

DFT calculations were employed to further investigate the charge distribution within each domain of the structure. The electrostatic potential (ESP) surfaces indicated positive ESP around the centroid of Cu(I) CTU, implying a favorable binding affinity between Cu(I) CTU and the electron-rich regions (C≡C bond) of substrates (Figure S34). Moreover, a bimolecular adduct model (Cu-CTU@**2a**) composed of the Cu-CTU region in CMOF and substrate **2a** was constructed, and an independent gradient model based on the Hirshfeld (IGMH) analysis of Cu-CTU@**2a** was performed. IGMH analysis revealed a clear interaction between the Cu site and the C≡C bond in **2a**, with a calculated binding energy of −13.95 kJ/mol for Cu-CTU@**2a** (Figure S35). To

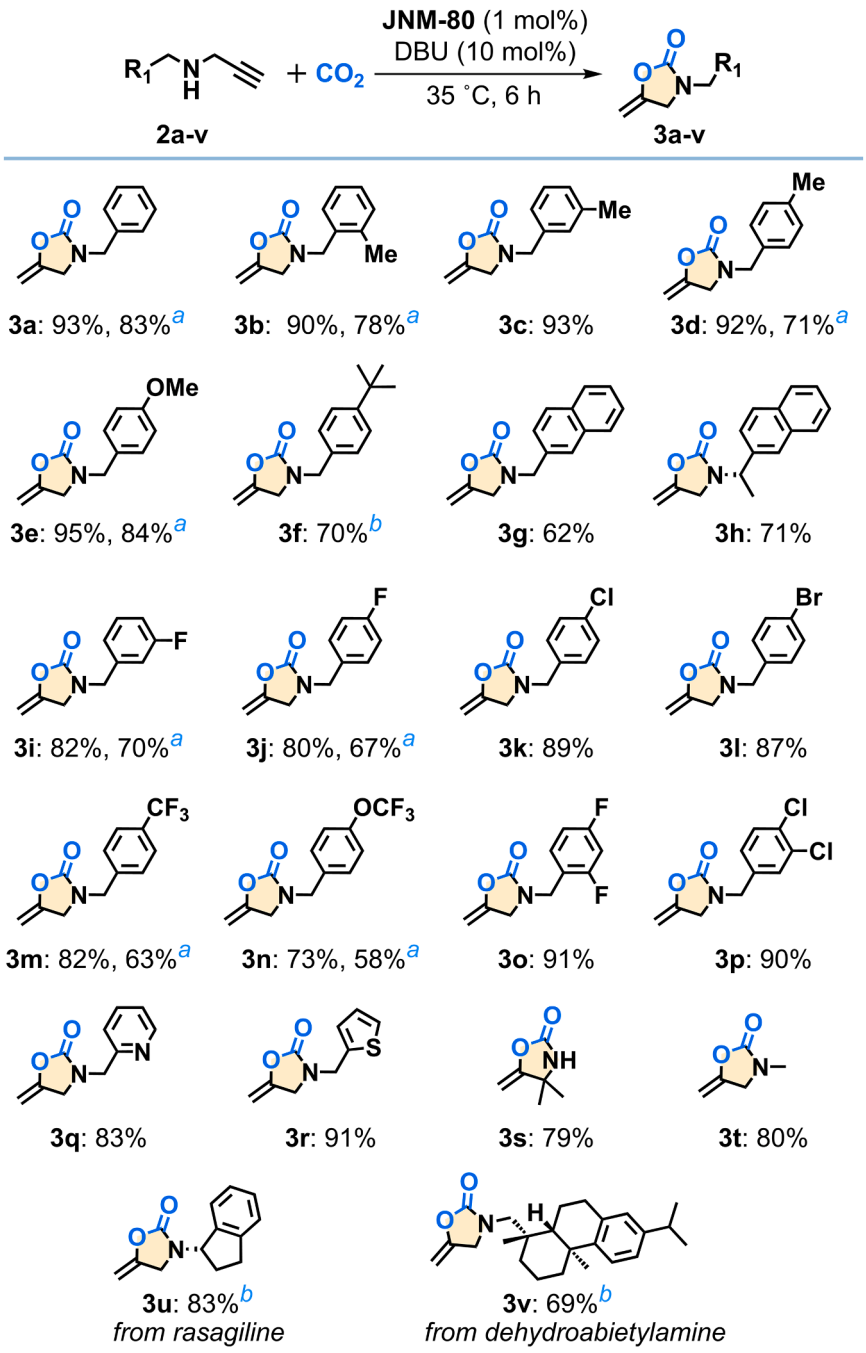


Figure 4. Substrate scope for carboxylative cyclization of propylamine with CO_2

Substrate scope of propargylamine. The standard reaction conditions are detailed in Table 1. All yields were determined by isolated products.
(A) CO_2: 25%, N_2: 70.5%, O_2: 4%, SO_2: 0.5%, P (1 atm), DBU (20 mol %), solvent-free, 60°C, 12 h. Catalyst was exposed to humid conditions (relative humidity [RH]: 90%) for 12 h before the reaction.
(B) 0.5 mL CH_3CN, 6 h.

elucidate the CO_2 adsorption behavior, we performed GCMC simulations to identify the preferred adsorption sites and density distributions across the four frameworks. The CO_2 binding sites can be classified into three categories depending on the local structural environment, dominated by O···M, O···H, and C···H interactions (Figures 5D, 5E, and S36–S39). Among the four materials, **JNM-80** displays the most diverse set of binding environments, including a dominant site (site 1) where CO_2 engages in a strong cooperative interaction with Cu-CTU units, enabling adsorption of up to 10 CO_2 molecules per unit cell (Figures 5E and S37; Table S12). In contrast, the homopore structure of FDM-71 restricts both the CO_2 adsorption density and the total number of adsorbed molecules (5 per unit cell), owing to fewer binding sites and the inefficient utilization of the pore volume (Figures 5D and S36; Table S12). Overall, **JNM-80** exhibited a higher CO_2 uptake capacity and stronger adsorption density, consistent with its superior experimental CO_2 adsorption and catalytic conversion performance. Based on the above experimental results and previous studies,[45–47] a plausible mechanism was proposed for the **JNM-80**-catalyzed cyclization reaction (Figure S30). First, DBU dehydrogenates the NH in **2a**, leading to the formation of a carbamate anion (II) via electrophilic attack of CO_2 on the nitrogen atom. Second, the Cu(I) in the CTU of **JNM-80** coordinates to and activates the C≡C bond of propargylamine, generating the intermediate state (III). Subsequently, intramolecular nucleophilic cyclization of III, facilitated by the **JNM-80**, yields a five-membered ring (IV) intermediate. Finally, the product (**3a**) is formed through proton migration from $DBUH^+$, and the catalyst and DBU were regenerated at the same time.

Conclusions

In summary, we synthesized three 2D heteropore CMOFs (e.g., **JNM-80**, **JNM-81**, and **JNM-82**) for the first time, employing a combination of metal-coordination and dynamic covalent Schiff-base condensation reactions. Among them, **JNM-80** exhibited a CO_2 adsorption capacity of 34.50 $cm^3\ g^{-1}$, more than double that of its homopore analog, FDM-71, and markedly enhanced its catalytic performance in the cyclization of propargylamine with CO_2 (TOF of 141.3 h^{-1} vs. 13.3 h^{-1} for FDM-71). Moreover, **JNM-80** surpasses FDM-71 in catalytic activity for the conversion of CO_2 to quinazoline-2,4(1*H*,3*H*)-dione, cyclization of epoxides, and

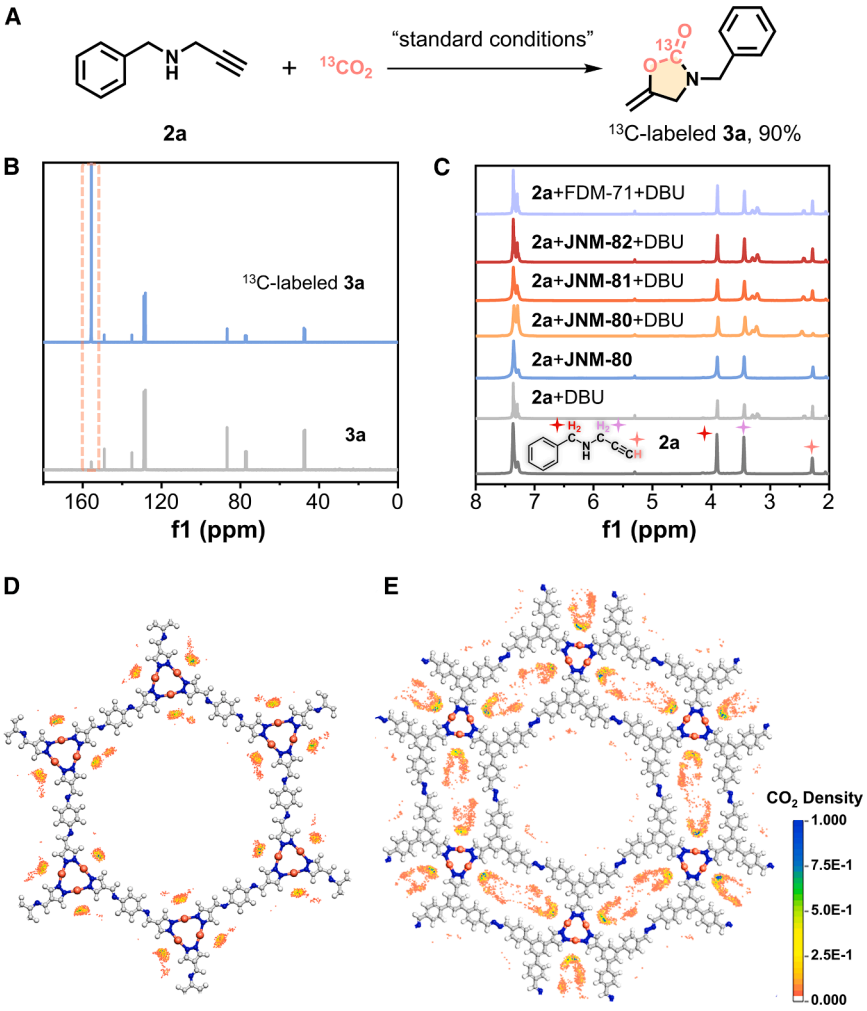


Figure 5. Mechanism studies and GCMC calculations

(A) ^{13}C-isotope labeling experiments.

(B) ^{13}C NMR (101 MHz, 298 K, $CDCl_3$) spectra of ^{13}C-labeled **3a** (top) and unlabeled **3a** (bottom).

(C) Activation of the **2a** by different systems (^1H NMR, 400 MHz, 298 K, $CDCl_3$).

(D and E) CO_2 density distribution for FDM-71 and **JNM-80**.

N-formylation of amines. **JNM-80** further demonstrated remarkable robustness, sustaining high yields (84%) under humid simulated flue gas and maintaining activity and structural integrity over seven cycles. Mechanistic studies combining NMR monitoring, isotope labeling, and DFT and GCMC calculations provided molecular-level insight into the catalytic process. Our work sets a precedent for the molecular-level design of 2D heteropore MOFs, establishing them as a versatile platform for developing high-performance catalysts for sustainable CO_2 conversion.

METHODS

Details regarding the experimental procedures can be found in the supplemental methods.

RESOURCE AVAILABILITY

Lead contact

Further information and requests for resources should be directed to and will be fulfilled by the lead contact, Guo-Hong Ning (guohongning@jnu.edu.cn).

Materials availability

The supplemental information file includes experimental sections (Figures S1–S33; Tables S1–S11), the calculated results (Figures S34–S39; Table S12), and the NMR spectra. All reagents in this study are either commercially available or can easily be prepared, as indicated in the supplemental information.

Data and code availability

All data for the replication of this work are given in the supplemental information or can be obtained by the lead contact upon reasonable request.

ACKNOWLEDGMENTS

This work was financially supported by the Guangdong Basic and Applied Basic Research Foundation (2024A1515010897), Fundamental Research Funds for the Central Universities (21624106), the National Natural Science Foundation of China (nos. 22371091, 22431006, and 92461309), and the Guangdong Major Project of Basic and Applied Research (no. 2019B030302009).

AUTHOR CONTRIBUTIONS

G.-H.N. and D.L. conceived and supervised the research; X.C. and Y.-Y.L. conducted the experiments and data analysis; and Z.-H.L. and J.-Y.S. contributed to the synthesis of ligands and materials. X.C. and R.-Q.X. contributed

to the DFT calculation; Y.-M.W. and C.-W.Z. contributed to material analysis; and Y.H. contributed to HR-TEM images of the material. H.-L.J. revised the manuscript. X.C., Y.-Y.L., G.-H.N., and D.L. co-wrote the manuscript. All authors read and commented on the manuscript.

DECLARATION OF INTERESTS

The authors declare no competing interests.

SUPPLEMENTAL INFORMATION

Supplemental information can be found online at https://doi.org/10.1016/j.chempr.2026.103006.

Received: November 18, 2025
Revised: January 12, 2026
Accepted: March 6, 2026
Published: March 30, 2026

REFERENCES

1. Sanz-Pérez, E.S., Murdock, C.R., Didas, S.A., and Jones, C.W. (2016). Direct capture of CO_2 from ambient air. Chem. Rev. *116*, 11840–11876. https://doi.org/10.1021/acs.chemrev.6b00173.
2. Lin, S., Diercks, C.S., Zhang, Y.-B., Kornienko, N., Nichols, E.M., Zhao, Y., Paris, A.R., Kim, D., Yang, P., Yaghi, O.M., et al. (2015). Covalent organic frameworks comprising cobalt porphyrins for catalytic CO_2 reduction in water. Science *349*, 1208–1213. https://doi.org/10.1126/science.aac8343.
3. Anagnostou, E., John, E.H., Edgar, K.M., Foster, G.L., Ridgwell, A., Inglis, G.N., Pancost, R.D., Lunt, D.J., and Pearson, P.N. (2016). Changing atmospheric CO_2 concentration was the primary driver of early Cenozoic climate. Nature *533*, 380–384. https://doi.org/10.1038/nature17423.
4. Aresta, M., Dibenedetto, A., and Angelini, A. (2014). Catalysis for the valorization of exhaust carbon: from CO_2 to chemicals, materials, and fuels. Technological use of CO_2. Chem. Rev. *114*, 1709–1742. https://doi.org/10.1021/cr4002758.
5. Ye, J.-H., Ju, T., Huang, H., Liao, L.-L., and Yu, D.-G. (2021). Radical carboxylative cyclizations and carboxylations with CO_2. Acc. Chem. Res. *54*, 2518–2531. https://doi.org/10.1021/acs.accounts.1c00135.
6. Cai, T., Sun, H., Qiao, J., Zhu, L., Zhang, F., Zhang, J., Tang, Z., Wei, X., Yang, J., Yuan, Q., et al. (2021). Cell-free chemoenzymatic starch synthesis from carbon dioxide. Science *373*, 1523–1527. https://doi.org/10.1126/science.abh4049.
7. Aresta, M., Dibenedetto, A., and Quaranta, E. (2016). Reaction Mechanisms in Carbon Dioxide Conversion (Springer Berlin Heidelberg). https://doi.org/10.1007/978-3-662-46831-9.
8. Wang, S., and Xi, C. (2019). Recent advances in nucleophile-triggered CO_2-incorporated cyclization leading to heterocycles. Chem. Soc. Rev. *48*, 382–404. https://doi.org/10.1039/C8CS00281A.
9. Hou, S.L., Dong, J., Zhao, X.Y., Li, X.S., Ren, F.Y., Zhao, J., and Zhao, B. (2023). Thermo-Catalysis of CO_2 into Valuable Products Activated by Noble-Metal-Free Metal-Organic Frameworks. Angew. Chem. Int. Ed. Engl. *62*, e202305213. https://doi.org/10.1002/anie.202305213.
10. Singh, G., Lee, J., Karakoti, A., Bahadur, R., Yi, J., Zhao, D., AlBahily, K., and Vinu, A. (2020). Emerging trends in porous materials for CO_2 capture and conversion. Chem. Soc. Rev. *49*, 4360–4404. https://doi.org/10.1039/D0CS00075B.
11. Ding, M., Flaig, R.W., Jiang, H.-L., and Yaghi, O.M. (2019). Carbon capture and conversion using metal–organic frameworks and MOF-based materials. Chem. Soc. Rev. *48*, 2783–2828. https://doi.org/10.1039/C8CS00829A.
12. Schoedel, A., Ji, Z., and Yaghi, O.M. (2016). The role of metal–organic frameworks in a carbon-neutral energy cycle. Nat. Energy *1*, 1–13. https://doi.org/10.1038/nenergy.2016.34.
13. Zou, Y.H., Huang, Y.B., Si, D.H., Yin, Q., Wu, Q.J., Weng, Z., and Cao, R. (2021). Porous metal–organic framework liquids for enhanced CO_2 adsorption and catalytic conversion. Angew. Chem. Int. Ed. Engl. *60*, 20915–20920. https://doi.org/10.1002/anie.202107156.
14. Wang, Y., Wei, J.-X., Tang, H.-L., Shao, L.-H., Dong, L.-Z., Chu, X.-Y., Jiang, Y.-X., Zhang, G.-L., Zhang, F.-M., and Lan, Y.-Q. (2024). Artificial photosynthetic system for diluted CO_2 reduction in gas-solid phase. Nat. Commun. *15*, 8818. https://doi.org/10.1038/s41467-024-53066-y.
15. Deng, S., Xiong, Y.-Y., Chen, C.-X., Dai, Q.-H., Chen, Y.-X., Geng, W., Liang, Z.-Y., Ruan, W.-L., Wei, Z.-W., Barboiu, M., et al. (2025). Achieving Diverse CO_2 Conversions through On-Demand Installation of Multivariate Catalytic Sites into One Prototypical Metal–Organic Framework. J. Am. Chem. Soc. *147*, 19996–20007. https://doi.org/10.1021/jacs.5c05028.
16. Zhang, C., Lin, Z., Jiao, L., and Jiang, H.L. (2024). Metal–organic frameworks for electrocatalytic CO_2 reduction: From catalytic site design to microenvironment modulation. Angew. Chem. Int. Ed. Engl. *63*, e202414506. https://doi.org/10.1002/anie.202414506.
17. Cai, G., Yan, P., Zhang, L., Zhou, H.C., and Jiang, H.L. (2021). Metal-Organic Framework-Based Hierarchically Porous Materials: Synthesis and Applications. Chem. Rev. *121*, 12278–12326. https://doi.org/10.1021/acs.chemrev.1c00243.
18. Pang, J., Zhang, Z., Zhang, S., Guo, X., Chen, Q., Zhang, X.-W., Zhou, H.-L., Gong, W., Shah, S.S.A., Zhong, C., et al. (2025). Recent progress in metal-organic frameworks: part I—material preparation. Sci. China Chem. *68*, 1230–1286. https://doi.org/10.1007/s11426-024-2457-y.
19. Chen, X., Song, J.-Y., Zheng, J., Wang, Y.-M., Luo, J., Weng, P., Cai, B.-C., Lin, X.-C., Ning, G.-H., and Li, D. (2024). Metal variance in multivariate metal–organic frameworks for boosting catalytic conversion of CO_2. J. Am. Chem. Soc. *146*, 19271–19278. https://doi.org/10.1021/jacs.4c04556.
20. Xu, H., Cao, C.S., Hu, H.S., Wang, S.B., Liu, J.C., Cheng, P., Kaltsoyannis, N., Li, J., and Zhao, B. (2019). High Uptake of ReO^{4-} and CO_2 Conversion by a Radiation-Resistant Thorium–Nickle $[Th_{48}Ni_6]$ Nanocage-Based Metal–Organic Framework. Angew. Chem. Int. Ed. Engl. *58*, 6022–6027. https://doi.org/10.1002/anie.201901786.
21. Gu, Y., Anjali, B.A., Yoon, S., Choe, Y., Chung, Y.G., and Park, D.-W. (2022). Defect-engineered MOF-801 for cycloaddition of CO_2 with epoxides. J. Mater. Chem. A *10*, 10051–10061. https://doi.org/10.1039/D2TA00503D.
22. Gu, A.L., Zhang, Y.X., Wu, Z.L., Cui, H.Y., Hu, T.D., and Zhao, B. (2022). Highly Efficient Conversion of Propargylic Alcohols and Propargylic Amines with CO_2 Activated by Noble-Metal-Free Catalyst Cu_2O@ZIF-8. Angew. Chem. Int. Ed. Engl. *61*, e202114817. https://doi.org/10.1002/anie.202114817.
23. Kajiwara, T., Fujii, M., Tsujimoto, M., Kobayashi, K., Higuchi, M., Tanaka, K., and Kitagawa, S. (2016). Photochemical reduction of low concentrations of CO_2 in a porous coordination polymer with a ruthenium (II). Angew. Chem. Int. Ed. Engl. *55*, 2697–2700. https://doi.org/10.1002/anie.201508941.
24. Forse, A.C., Colwell, K.A., Gonzalez, M.I., Benders, S., Torres-Gavosto, R.M., Blümich, B., Reimer, J.A., and Long, J.R. (2020). Influence of pore size on carbon dioxide diffusion in two isoreticular metal–organic frameworks. Chem. Mater. *32*, 3570–3576. https://doi.org/10.1021/acs.chemmater.0c00745.
25. Wang, K.-Y., Yang, Z., Zhang, J., Banerjee, S., Joseph, E.A., Hsu, Y.-C., Yuan, S., Feng, L., and Zhou, H.-C. (2023). Creating hierarchical pores in metal–organic frameworks via postsynthetic reactions. Nat. Protoc. *18*, 604–625. https://doi.org/10.1038/s41596-022-00759-7.
26. Su, X., Zhong, Z., Yan, X., Zhang, T., Wang, C., Wang, Y.X., Xu, G., and Chen, L. (2023). Facile Synthesis of Metallosalphen-Based 2D Conductive Metal-Organic Frameworks for NO_2 Sensing: Metal Coordination Induced

Planarization. Angew. Chem. Int. Ed. Engl. *62*, e202302645. https://doi.org/10.1002/anie.202302645.

27. Zhou, T.-Y., Xu, S.-Q., Wen, Q., Pang, Z.-F., and Zhao, X. (2014). One-step construction of two different kinds of pores in a 2D covalent organic framework. J. Am. Chem. Soc. *136*, 15885–15888. https://doi.org/10.1021/ja5092936.
28. Feng, B., Chen, X., Yan, P., Huang, S., Lu, C., Ji, H., Zhu, J., Yang, Z., Cao, K., and Zhuang, X. (2023). Isomeric Dual-Pore Two-Dimensional Covalent Organic Frameworks. J. Am. Chem. Soc. *145*, 26871–26882. https://doi.org/10.1021/jacs.3c09559.
29. Mu, Z., Zhu, Y., Zhang, Y., Dong, A., Xing, C., Niu, Z., Wang, B., and Feng, X. (2023). Hierarchical Microtubular Covalent Organic Frameworks Achieved by COF-to-COF Transformation. Angew. Chem. Int. Ed. Engl. *62*, e202300373. https://doi.org/10.1002/anie.202300373.
30. Sun, Q., Aguila, B., Lan, P.C., and Ma, S. (2019). Tuning Pore Heterogeneity in Covalent Organic Frameworks for Enhanced Enzyme Accessibility and Resistance against Denaturants. Adv. Mater. *31*, e1900008. https://doi.org/10.1002/adma.201900008.
31. Liang, R.-R., Jiang, S.-Y., A, R.-H., and Zhao, X. (2020). Two-dimensional covalent organic frameworks with hierarchical porosity. Chem. Soc. Rev. *49*, 3920–3951. https://doi.org/10.1039/D0CS00049C.
32. Qian, C., and Zhao, X. (2025). Two-Dimensional Heteropore Covalent Organic Frameworks: From Construction to Functions. Acc. Chem. Res. *58*, 1192–1209. https://doi.org/10.1021/acs.accounts.4c00799.
33. Qian, C., Qi, Q.-Y., Jiang, G.-F., Cui, F.-Z., Tian, Y., and Zhao, X. (2017). Toward covalent organic frameworks bearing three different kinds of pores: the strategy for construction and COF-to-COF transformation via heterogeneous linker exchange. J. Am. Chem. Soc. *139*, 6736–6743. https://doi.org/10.1021/jacs.7b02303.
34. Liang, R.-R., Xu, S.-Q., Zhang, L., A, R.-H., Chen, P., Cui, F.-Z., Qi, Q.-Y., Sun, J., and Zhao, X. (2019). Rational design of crystalline two-dimensional frameworks with highly complicated topological structures. Nat. Commun. *10*, 4609. https://doi.org/10.1038/s41467-019-12596-6.
35. Wei, R.-J., Zhou, H.-G., Zhang, Z.-Y., Ning, G.-H., and Li, D. (2021). Copper(I)–Organic Frameworks for Catalysis: Networking Metal Clusters with Dynamic Covalent Chemistry. CCS Chem. *3*, 2045–2053. https://doi.org/10.31635/ccschem.020.202000401.
36. Wei, R.-J., You, P.-Y., Duan, H., Xie, M., Xia, R.-Q., Chen, X., Zhao, X., Ning, G.-H., Cooper, A.I., and Li, D. (2022). Ultrathin metal–organic framework nanosheets exhibiting exceptional catalytic activity. J. Am. Chem. Soc. *144*, 17487–17495. https://doi.org/10.1021/jacs.2c06312.
37. Wei, R.-J., Luo, X., Ning, G.-H., and Li, D. (2025). Covalent Metal–Organic Frameworks: Fusion of Covalent Organic Frameworks and Metal–Organic Frameworks. Acc. Chem. Res. *58*, 746–761. https://doi.org/10.1021/acs.accounts.4c00774.
38. Luo, J., Lin, J.T., Luo, X., Yin, N., Xie, M., Chen, X., Li, Y.Q., Li, Y.G., Ning, G.H., and Li, D. (2025). Cyclic Trinuclear Units Based Covalent Metal-Organic Frameworks for Gold Recovery. Angew. Chem. Int. Ed. Engl. *64*, e202502749. https://doi.org/10.1002/anie.202502749.
39. Xia, R.Q., Liu, Z.N., Tang, Y.Y., Wu, T., Luo, X., Deng, Q.M., Ning, G.H., and Li, D. (2025). In Situ Exfoliation of Covalent Metal-Organic Frameworks for Enhancing Photocatalytic Hydrogen Peroxide Production. Angew. Chem. Int. Ed. Engl. *64*, e202514091. https://doi.org/10.1002/anie.202514091.
40. Li, X., Wang, J., Xue, F., Wu, Y., Xu, H., Yi, T., and Li, Q. (2021). An imine-linked metal–organic framework as a reactive oxygen species generator. Angew. Chem. Int. Ed. Engl. *60*, 2534–2540. https://doi.org/10.1002/anie.202012947.
41. Duan, J., Teng, L., Liu, H., Zhang, X., Yu, H., Huang, Q., Li, Y., Liu, M., Hu, H., Lyu, W., et al. (2025). Heteroporous Donor-Acceptor Covalent Organic Framework Cathode for High-Rate-Capacity Lithium-Ion Battery. Angew. Chem. Int. Ed. Engl. *64*, e202517853. https://doi.org/10.1002/anie.202517853.
42. Yang, M., Zhang, Y., Zhu, R., Tan, J., Liu, J., Zhang, W., Zhou, M., and Meng, Z. (2024). Two-Dimensional Conjugated Metal–Organic Frameworks with a Ring-in-Ring Topology and High Electrical Conductance. Angew. Chem. Int. Ed. Engl. *63*, e202405333. https://doi.org/10.1002/anie.202405333.
43. Samanta, S., and Srivastava, R. (2020). Catalytic conversion of CO_2 to chemicals and fuels: the collective thermocatalytic/photocatalytic/electrocatalytic approach with graphitic carbon nitride. Mater. Mater. Adv. *1*, 1506–1545. https://doi.org/10.1039/D0MA00293C.
44. Wei, S., Zhang, L., Liu, S., Zhang, H., Huang, Y., Wan, L., Sun, Z., Liao, B., Wang, M., and Lu, X. (2025). Enhanced selective CO_2 adsorption in MOFs: Balance between open metal sites concentration and pore size. Sep. Purif. Technol. *377*, 134465. https://doi.org/10.1016/j.seppur.2025.134465.
45. Li, L., Lv, Y., Sheng, H., Du, Y., Li, H., Yun, Y., Zhang, Z., Yu, H., and Zhu, M. (2023). A low-nuclear Ag_4 nanocluster as a customized catalyst for the cyclization of propargylamine with CO_2. Nat. Commun. *14*, 6989. https://doi.org/10.1038/s41467-023-42723-3.
46. Jiang, X.L., Jiao, Y.E., Hou, S.L., Geng, L.C., Wang, H.Z., and Zhao, B. (2021). Green conversion of CO_2 and propargylamines triggered by triply synergistic catalytic effects in metal–organic frameworks. Angew. Chem. Int. Ed. Engl. *60*, 20417–20423. https://doi.org/10.1002/anie.202106773.
47. Chang, Z., Jing, X., He, C., Liu, X., and Duan, C. (2018). Silver Clusters as Robust Nodes and π–A ctivation Sites for the Construction of Heterogeneous Catalysts for the Cycloaddition of Propargylamines. ACS Catal. *8*, 1384–1391. https://doi.org/10.1021/acscatal.7b02844.